Whitening of odor representations by the wiring diagram of the olfactory bulb

Adrian A. Wanner[1,2,†], Rainer W. Friedrich[1,2,*]

[1]Friedrich Miescher Institute for Biomedical Research, Maulbeerstrasse 66, 4058 Basel, Switzerland

[2]Faculty of Natural Sciences, University of Basel, 4003 Basel, Switzerland

*Correspondence to: R. Friedrich, Friedrich Miescher Institute for Biomedical Research, Maulbeerstrasse 66, 4058 Basel, Switzerland

†Current address: Princeton Neuroscience Institute, Princeton University, 20 Washington Road, 08544 Princeton, New Jersey, USA

Neuronal computations underlying higher brain functions depend on synaptic interactions among specific neurons. A mechanistic understanding of such computations requires wiring diagrams of neuronal networks. We examined how the olfactory bulb (OB) performs 'whitening', a fundamental computation that decorrelates activity patterns and supports their classification by memory networks. We measured odor-evoked activity in the OB of a zebrafish larva and subsequently reconstructed the complete wiring diagram by volumetric electron microscopy. The resulting functional connectome revealed an overrepresentation of multisynaptic connectivity motifs that mediate reciprocal inhibition between neurons with similar tuning. This connectivity suppressed redundant responses and was necessary and sufficient to reproduce whitening in simulations. Whitening of odor representations is therefore mediated by higher-order structure in the wiring diagram that is adapted to natural input patterns.

Neuronal activity patterns evoked by natural stimuli are transformed in the brain to extract relevant information. Such patterns often contain correlations and intensity variations that originate from the statistics of natural scenes and from the tuning of sensory receptors[1]. This statistical structure complicates the classification of sensory inputs because it does not usually reflect behaviorally relevant stimulus categories[2]. For example, visual scenes may be dominated by a large number of pixels representing sky while the biologically most important information is conveyed by a small subset of pixels representing specific objects (e.g., a hawk or a sparrow). Hence, correlations in sensory inputs can complicate meaningful pattern classification and object recognition. This problem can be alleviated by whitening, a fundamental transformation in signal processing that decorrelates patterns and normalizes their variance. Whitening is therefore often used early in a pattern classification process to remove undesired correlations and to optimize the use of coding space[3].

In the visual and auditory system, whitening of individual neurons' responses to natural stimuli supports efficient coding by redundancy reduction[4-7]. Efficient pattern classification, however, requires whitening of activity patterns across neuronal populations. This form of whitening occurs in the olfactory bulb (OB)[8-10] where axons of olfactory sensory neurons expressing the same odorant receptor converge onto discrete glomeruli. Odors evoke distributed patterns of input activity across array of glomeruli that can overlap substantially when odorants share functional groups[11-13]. Moreover, the variance (contrast) of glomerular activity patterns varies dramatically as a function of odor concentration. As a consequence, patterns of sensory input to the OB are not well suited for concentration-invariant odor classification. The output of the OB is transmitted to higher brain areas by mitral cells, which receive sensory input from individual glomeruli and interact with other mitral cells via multisynaptic interneuron (IN) pathways (Fig. 1a). Contrary to glomerular inputs, activity patterns across mitral cells become rapidly decorrelated during the initial phase of an odor response[8,14-18] and their variance depends only modestly on stimulus intensity[10,19]. Neuronal circuits in the OB therefore decorrelate and normalize population activity patterns,

50 resulting in a whitening of odor representations that facilitates pattern classification. However, it remains
51 unclear how this transformation is achieved by interactions between neurons in the OB network.

52 Efficient whitening can be achieved by transformations that are adapted to the correlation structure of
53 input patterns[1]. Such adaptive whitening requires prior knowledge about inputs and tuning-dependent
54 connectivity between specific cohorts of neurons. Hence, whitening of sensory representations is thought
55 to depend on an evolutionary memory of stimulus space that is contained in the wiring diagram of
56 neuronal circuits. This hypothesis is difficult to test in the OB because tuning and functional connectivity
57 cannot be inferred from topographical relationships between neurons[11,20-22]. Moreover, because
58 interactions between mitral cells are multisynaptic via INs, relevant inhibitory interactions cannot be
59 visualized by transsynaptic tracing across a single synapse.

60 Adaptive whitening and other memory-based processes are likely to depend on higher-order features of
61 neuronal connectivity that cannot be detected by sparse sampling of pairwise connectivity between
62 individual neurons. We therefore used a "functional connectomics" approach that combines population-
63 wide neuronal activity measurements with dense reconstructions of wiring diagrams. To achieve this goal
64 we took advantage of the small size of the larval zebrafish brain. We first measured odor responses of
65 neurons in the OB by multiphoton calcium imaging and subsequently reconstructed the synaptic
66 connectivity among all neurons by serial block-face scanning electron microscopy (SBEM)[23-26]. We found
67 that higher-order features of multisynaptic connectivity specifically suppress the activity of correlated
68 mitral cell ensembles in a stimulus-dependent manner, resulting in a decorrelation and variance
69 normalization. The wiring diagram of the OB is therefore adapted to the correlation structure of its inputs
70 and mediates a whitening operation based on contrast reduction rather than contrast enhancement.

71

72 **Results**

73 **Reconstruction of the wiring diagram and mapping of neuronal activity**

74 We previously acquired an SBEM image stack of the OB in a zebrafish larva and reconstructed 98% of
75 the neurons in the OB[25,26]. We now annotated the synaptic connections of all OB neurons to reconstruct
76 the full wiring diagram. Human annotators followed each of the reconstructed skeletons and manually
77 labeled all input and output synapses (Fig. 1b,c). Subsequently, synapses of INs were annotated a second
78 time by different annotators. Hence, each synapse involved in MC-IN-MC connectivity motifs should
79 have been encountered at least three times. To obtain a conservative estimate of the wiring diagram with
80 few false positives we retained only those synapses that were annotated at least twice by independent
81 annotators.

82 Each synapse was assigned a unitary weight so that the total connection strength between a pair of
83 neurons equaled the number of synapses. The resulting wiring diagram contained 19,874 MC→IN
84 synapses, 17,524 MC←IN synapses (Fig. 1d), and 13,610 synapses between INs. We also observed
85 contact sites between MCs associated with the same glomerulus where plasma membranes showed strong
86 staining but these sites usually lacked associated vesicles. We did therefore not consider synaptic
87 connections between MCs. On average, connected pairs of MCs and INs made 3.1 MC→IN synapses and
88 2.9 MC←IN synapses per pair. A hallmark of synaptic connectivity in the adult OB are reciprocal
89 dendrodendritic synaptic connections between the same MC-IN pair. In the larval OB, 52% of MC→IN
90 synapses and 51% of MC←IN synapses were associated with a synapse of opposite direction, usually
91 within 2.5 μm, between the same pair of neurons (Fig. 1b, bottom). Hence, reciprocal synaptic
92 connectivity is prominent already in the larval OB of zebrafish.

93 Prior to preparation of the OB sample for SBEM we measured neuronal activity by multiphoton imaging
94 of the calcium indicator GCaMP5, which was expressed under the pan-neuronal elavl3 promoter[27].
95 Somata observed in electron microscopy were mapped onto the light microscopy data using an iterative
96 landmark-based affine alignment procedure followed by manual proofreading (Fig. 2a,b; Supplementary

97 Fig. 1). Somatic calcium signals evoked by four amino acid odors (10^{-4} M) and four bile acid odors
98 (10^{-5} M) were measured sequentially in six optical planes (Fig. 2a; Supplementary Fig. 1) and temporally
99 deconvolved to estimate odor-evoked firing rate changes[28]. The dynamics of neuronal population activity
100 was then represented by time series of activity vectors for each odor stimulus (232 MCs and 68 INs).

101 Decorrelation and contrast normalization of activity patterns across MCs have been characterized
102 previously in the OB of adult zebrafish[8,14,15] and mice[16-18] where >90% of neurons are GABAergic INs. In
103 the larval OB, in contrast, INs account for only 25% of all neurons[26]. Most of these INs are likely to be
104 periglomerular and short axon cells because INs with the typical morphology of granule cells appear only
105 later in development. We therefore asked whether the core circuitry present in the larval OB already
106 performs computations related to whitening.

107 Correlations between activity patterns evoked by different bile acids were high after stimulus onset and
108 decreased during the subsequent few hundred milliseconds (Fig. 2d,e). Patterns evoked by amino acids, in
109 contrast, were less correlated throughout the odor response, which was expected because most amino
110 acids had dissimilar side chains. To quantify pattern decorrelation we focused on activity patterns evoked
111 by bile acids and computed the mean difference in pairwise Pearson correlations between a time window
112 shortly after response onset (t_1) and a later time window (t_2). Time windows were chosen such that the
113 mean population activity across MCs was not significantly different (Fig. 2d; $p = 0.44$, Wilcoxon rank-
114 sum test). Pattern correlations across MCs, however, were significantly lower at t_2 than at t_1 ($p = 0.03$,
115 Wilcoxon rank-sum test), demonstrating that MC activity patterns were reorganized and decorrelated.
116 Activity across INs followed the mean MC activity with a small delay and did not exhibit an obvious
117 decorrelation (Fig. 2d), consistent with observations in the adult OB[29].

118 The contrast of MC activity patterns, as measured by the variance of activity across the population,
119 increased shortly after stimulus onset and peaked slightly later than the pattern correlation. Subsequently,
120 variance decreased and became more uniform across odors, as reflected by a significant decrease in the

121 standard deviation of the variance across odors between t_2 and t_1 (Fig. 2d; $p < 0.01$, Wilcoxon rank-sum
122 test; t_1 was slightly shifted relative to the time window for correlation analysis to cover the peak of the
123 variance). Hence, MC activity patterns in the larval OB became decorrelated and contrast-normalized,
124 consistent with the whitening of odor representations in the adult OB.

125

126 **Computational consequences of connectivity**

127 While contrast normalization can be achieved by global scaling operations such as divisive
128 normalization[30], pattern decorrelation requires interactions between distinct subsets of neurons[9]. In theory,
129 pattern decorrelation could be achieved by large networks with sparse and random connectivity[31] but this
130 architecture is inconsistent with the low number of INs in the larval OB. Smaller networks can decorrelate
131 specific input patterns when their connectivity is specifically adapted to the structure of sensory inputs,
132 suggesting that decorrelation in the OB is an input-specific transformation of odor representations that is
133 encoded in the wiring diagram. In order to explore this hypothesis we first asked whether whitening can
134 be reproduced by implementing the wiring diagram in a network of minimally complex single-neuron
135 models (Fig. 3a).

136 We simulated a network of threshold-linear rate neurons with 208 MCs, representing all recorded MCs
137 with input and output synapses, and 234 INs, representing all connected INs. Connections between MCs
138 and INs were given by the wiring diagram and excitatory sensory input into MCs was given by the odor-
139 evoked activity pattern at t_1. For simplicity, IN-IN connections were not considered. The time course of
140 stimuli consisted of a fast initial rise followed by a slow decay[31], approximating the response time course
141 of olfactory sensory neurons in zebrafish[8]. Because connectivity was fixed, the final network model had
142 only six degrees of freedom (thresholds, synaptic weight scaling factors and time constants of each
143 neuron type).

144 Correlations between simulated population responses to bile acids increased rapidly and subsequently
145 decreased. Consistent with experimental observations, the mean correlation decreased significantly
146 between two time windows t_1 and t_2 that were chosen so that the mean activity was not significantly
147 different (Fig. 3b,c). The variance (contrast) of activity patterns and its standard deviation across stimuli
148 followed a similar time course but peaked slightly later than the correlation, consistent with experimental
149 observations. Both measures decreased significantly between t_1 and t_2 (Fig. 3b,c; t_1 was adjusted slightly
150 to cover the peak of the variance). Hence, a minimal network implementing the reconstructed
151 connectivity reproduced whitening of biologically realistic inputs. When connectivity was randomized,
152 decorrelation and contrast normalization were both abolished (Fig. 4b-d). We therefore conclude that
153 whitening depended on the wiring diagram.

154 To further confirm this conclusion we examined whether the reorganization of activity patterns
155 underlying whitening can be predicted from connectivity without an explicit simulation of network
156 dynamics. Activity patterns at t_1 were multiplied with the feed-forward connectivity $W_{MC \rightarrow IN}$ and
157 thresholded to generate a hypothetical pattern of IN activity. This activity pattern was then multiplied
158 with the feed-back connectivity $W_{MC \leftarrow IN}$ to predict the pattern of feedback inhibition, which was
159 subtracted from t_1. This simple algebraic procedure reproduced both pattern decorrelation and variance
160 normalization (Fig. 3c) but failed to do so when connectivity matrices were randomized (not shown),
161 further supporting the conclusion that the wiring diagram contains specific information essential for
162 whitening.

163 We next performed more specific manipulations to explore how whitening depends on higher-order
164 structure in the wiring diagram. In simulations, we first applied the same permutations to the feed-forward
165 (MC→IN) and feed-back connectivity (MC←IN). This manipulation shuffles the off-diagonal elements
166 in the disynaptic connectivity matrix (lateral inhibition) but preserves the overall distribution of
167 disynaptic MC→IN→MC connection strengths and the on-diagonal elements (self-inhibition; Fig. 3d).

168 Similar to the full randomization of connectivity, this co-permutation abolished whitening (Fig. 3b,c).
169 Moreover, whitening was abolished when input channels were permuted to produce novel input patterns
170 with the same statistical properties and correlations (Fig. 3c). These results show that whitening is
171 mediated by higher-order features of multisynaptic connectivity that are adapted to patterns of sensory
172 input.

173

174 **Mechanisms of whitening**

175 The shortest path between MCs associated with different glomeruli is a disynaptic interaction via one IN
176 (MC-IN-MC). To identify properties of the wiring diagram that mediate whitening we therefore analyzed
177 MC-IN-MC triplets. There are nine possible triplet configurations that represent four topological motifs
178 (Fig. 4a). We found that the motif containing no reciprocal connection (motif 1) was underrepresented
179 whereas the other motifs were overrepresented in comparison to randomized networks (Fig 4b). The
180 strongest overrepresentation was observed for motif 4, which contains reciprocal connections between
181 both MCs and the IN. Hence, MC-IN-MC triplets frequently contained reciprocal connections.

182 To determine whether disynaptic connectivity between MCs depends on their tuning we constructed an
183 input tuning curve for each MC from the responses to the eight odors at t_1. For all pairs of MCs we then
184 quantified the Pearson correlation between their input tuning curves and the number of disynaptic MC-
185 IN-MC connection paths across all motifs. The mean number of disynaptic connections increased with the
186 input tuning correlation (Fig. 4c). Hence, triplets mediate interactions preferentially between MCs with
187 similar tuning.

188 We further analyzed the relationship between triplet motifs and tuning curve similarity. Motifs with
189 reciprocal connections (motifs 2 – 4) were significantly overrepresented among MCs with similar tuning
190 (correlation >0.5; Fig. 4d). This overrepresentation was most pronounced for motif 4 (all connections

191 reciprocal). Hence, disynaptic reciprocal interactions are significantly enriched between MCs with similar
192 tuning.

193 In the retina, unidirectional lateral inhibition between functionally related neurons sharpens tuning curves
194 and enhances pattern contrast[32] (Fig. 5a, left). In idealized networks with strictly reciprocal connectivity,
195 in contrast, inhibition does not amplify asymmetries in inputs and self-inhibition is usually larger than
196 lateral inhibition (assuming equal synaptic strength; Fig. 5a, right). Hence, reciprocal triplet connectivity
197 among neurons with similar tuning should primarily down-regulate, rather than sharpen, the activity of
198 connected cohorts of neurons. The computational effects of these transformations depend on the
199 properties of input patterns (Supplementary Fig. 2). When inputs follow overlapping Gaussian
200 distributions, contrast enhancement can decorrelate patterns because stimulus-specific information is
201 contained in strong neuronal responses[4,32]. However, when activity patterns overlap primarily in strongly
202 responsive units, contrast enhancement will fail to decorrelate patterns because it emphasizes non-specific
203 responses. In this scenario, patterns may be decorrelated by the selective inhibition of strongly active
204 cohorts, which may be achieved by specific reciprocal inhibition (Supplementary Fig. 2).

205 To examine the basis of pattern correlations in the OB we analyzed population activity patterns evoked by
206 bile acids at t_1. For each pair of patterns, we quantified the contribution $r_{i,t1}$ of MC i to the Pearson
207 correlation r. Overall pattern correlations were dominated by high contributions from a small fraction of
208 MCs. This subset of MCs was also strongly active, as observed directly when MCs were ranked by their
209 $r_{i,t1}$ (Fig. 5b,c). As a corollary, these MCs also made large contributions to the variance of neuronal
210 activity patterns at t_1 (Fig. 5c). Hence, correlated odor representations overlapped primarily in strongly
211 responsive MCs, consistent with observations in the adult OB[9].

212 We then examined the changes in the activity of individual neurons underlying the decorrelation and
213 contrast normalization between t_1 and t_2. The activity of MCs with large $r_{i,t1}$ was significantly lower at t_2
214 than at t_1 (Fig. 5b,c). The activity of MCs that did not strongly contribute to the initial correlation, in

contrast, remained similar. As a consequence, the contribution of MCs with large $r_{i,t1}$ to the overall correlation decreased, resulting in a substantial decorrelation of population activity patterns between t_1 and t_2. Pattern decorrelation can therefore be attributed, at least in part, to the selective inhibition of MC cohorts that dominate the initial pattern correlations. MCs with high $r_{i,t1}$ also made strong contributions to pattern variance at t_1 (Fig. 5c) because their activity was substantially higher than the population mean. The selective inhibition of these cohorts between t_1 and t_2 changed the activity of these MCs towards the population mean and therefore decreased pattern variance and its s.d. across odors. Pattern decorrelation and contrast normalization can therefore be attributed to a common mechanism that targets inhibition to specific MC cohorts and results in contrast reduction rather than contrast enhancement.

The selective suppression of activity in cohorts of co-responsive MCs requires inhibition within cohorts to be stronger than the mean inhibition across the population. To explore how such stimulus- and ensemble-specific inhibition can arise from the connectivity between neurons we selected the 10 MCs with the highest $r_{i,t1}$ for each pair of bile acid stimuli. We then determined the disynaptic MC inputs to these cohorts by retrograde tracing through the wiring diagram across two synapses. Inputs to MCs within a cohort were strongly biased towards MCs of the same cohort (Fig. 5d,e), implying that neurons in a cohort will be strongly inhibited when the cohort is activated as a whole. The specific suppression of activity underlying whitening can therefore be explained by dense reciprocal connectivity within cohorts, which suppresses the representation of stimulus features that activate a cohort.

To further explore this hypothesis we continued to analyze the mechanism of whitening in simulations. We first ranked simulated MCs by their $r_{i,t1}$ for bile acid-evoked activity patterns in experiments (same ranking as in Fig. 5c). As observed experimentally, simulated MCs with large $r_{i,t1}$ were strongly inhibited between t_1 and t_2 while the mean activity of other MCs remained unchanged (Fig. 6a). Simulations therefore recapitulated the mechanism of whitening in the OB and precisely predicted the underlying activity changes in individual neurons.

239 We then selected the 10 MCs with the highest $r_{i,t1}$ for each pair of bile acid stimuli (19 MCs in total) and
240 deleted their feedforward connections onto INs in the simulation (11% of all MC→IN connections;
241 Fig. 6b, left). As a control, we deleted the same fraction of feedforward connections between random
242 subsets of neurons. While random deletions had almost no effect, the selective disconnection of functional
243 cohorts abolished pattern decorrelation and variance normalization (Fig. 6c,d). Ranking of MCs by their
244 $r_{i,t1}$ in experimental data demonstrated that the activity of MCs with high $r_{i,t1}$ was reduced slightly
245 between t_1 and t_2 when MC cohorts were selectively disconnected but not as effectively as under control
246 conditions. As a consequence, these MCs continued to make large positive contributions to pattern
247 correlation and variance at t_2 (Fig. 6e). These results show that the selective disconnection of functional
248 cohorts abolished whitening because it disrupted feature suppression. We next randomized all
249 connections except those of the 10 MCs with the highest $r_{i,t1}$ for each bile acid pair (Fig. 6b, right).
250 Results were compared to the full randomization of the wiring diagram, which reduced the inhibition of
251 MC cohorts and abolished whitening (Fig. 3b,c). When connections of functional MC cohorts were
252 selectively preserved, however, the inhibition of MC cohorts remained strong and pattern decorrelation
253 was restored (Fig. 6c,d). Variance normalization was only partially rescued, presumably because
254 preserved cohorts were selected only for their contribution to correlations between bile acid pairs and not
255 for amino acids. The activity of MCs with high $r_{i,t1}$ was strongly reduced (Fig. 6e), demonstrating that
256 pattern decorrelation and partial variance normalization were the result of feature suppression. These
257 results confirm that whitening is mediated by specific disynaptic interactions that suppress the activity of
258 correlation-promoting MC cohorts.

259

260 **Discussion**

261 We used a functional connectomics approach in a small vertebrate to explore the mechanism of whitening
262 in the OB. Whitening is a computation related to object classification and associative memory that

263 requires specific transformations of defined neuronal activity patterns. Such computations are thought to
264 rely on specific wiring diagrams that are adapted to relevant inputs. Consistent with this notion, we found
265 that whitening is achieved by specific multisynaptic interactions that cannot be described by general
266 topographic principles or by the first-order statistics of connectivity between neuron types. Functional
267 connectomics is therefore a promising approach to dissect distributed, memory-based computations
268 underlying higher brain functions.

269 Correlations between input patterns in the OB were dominated by distinct subsets of strongly active input
270 channels. This correlation structure is likely to reflect the co-activation of different odorant receptors by
271 discrete functional groups[12,13] and implies that input correlations cannot be removed efficiently by
272 contrast enhancement[33-35]. Rather, patterns are decorrelated by the selective inhibition of strongly active,
273 correlation-promoting MC cohorts. Pattern decorrelation is therefore achieved by contrast reduction,
274 rather than contrast enhancement, which also supports contrast normalization.

275 Whitening requires specific tuning-dependent, disynaptic MC-IN-MC connectivity that may be
276 established by molecular or activity-dependent mechanisms. Because this connectivity exists already
277 before activity-dependent effects were detected on the morphological development of glomeruli[36] the
278 initial assembly of neuronal connections may rely primarily on molecular cues. Projections of INs are
279 enriched between glomeruli that receive input from odorant receptors of the same families[26], raising the
280 possibility that glomerular targeting of sensory neurons[37] and INs involve related mechanisms. However,
281 the development of the connectivity that mediates whitening remains to be explored.

282 Lateral inhibition between neurons with similar tuning is often assumed to sharpen tuning curves by
283 amplifying asymmetries in the input. In the OB, however, triplet connections between related MCs are
284 highly enriched in reciprocal connections. This connectivity results in feedback inhibition that is
285 independent of the precise pattern of MC input to a cohort (Fig. 5a, right) and down-scales the activity of
286 neuronal cohorts without amplifying asymmetries in the input. Reciprocally connected MC↔IN↔MC

287 cohorts therefore mediate feature suppression: in the presence of a feature that effectively activates a
288 cohort, the inhibitory feedback gain within the cohort will be larger than the mean feedback gain and
289 suppress the representation of the feature. This mechanism can explain the selective and odor-dependent
290 inhibition of correlation-promoting MC cohorts.

291 Functional connectomics permitted us to test the significance of this mechanism by implementing the
292 wiring diagram in a network of minimally complex model neurons. Simulations demonstrated that higher-
293 order features of connectivity were necessary and sufficient to produce whitening. Precisely targeted
294 manipulations confirmed that whitening was the result of feature suppression by reciprocal
295 MC↔IN↔MC connectivity among correlation-promoting MC cohorts. Whitening in the OB is therefore
296 produced by a network mechanism that differs from canonical computations in the retina and other
297 sensory systems, presumably because the statistics of sensory inputs differ between sensory modalities.

298 In visual cortex, functionally related principal neurons make stronger excitatory connections than random
299 subsets of neurons[38]. Such connectivity can arise from Hebbian plasticity mechanisms, enhance
300 representations of sensory features, and amplify specific inputs in memory networks after learning. The
301 disynaptic connectivity observed in the OB, in contrast, results in inhibitory interactions between
302 functionally related principal neurons. Such connectivity cannot be achieved by monosynaptic
303 connectivity between MCs because inhibitory synapses between MCs would violate Dale's law.
304 Functional connectivity in the OB is therefore similar in structure, but opposite in sign, to excitatory
305 connectivity motifs in visual cortex. As a consequence, the connectivity in the OB suppresses, rather than
306 amplifies, specific features in the input. Such a mechanism appears useful to attenuate the impact of
307 irrelevant sensory inputs and to reduce undesired correlations. The mechanism of whitening by feature
308 suppression is consistent with networks that have been optimized for whitening in a theoretical
309 framework with biologically plausible constraints[39,40]. Hence, the mechanism of whitening observed in
310 the OB may represent a general computational strategy in the brain.

References

1 Simoncelli, E. P. & Olshausen, B. A. Natural image statistics and neural representation. *Annu Rev Neurosci* **24**, 1193-1216 (2001).

2 DiCarlo, J. J., Zoccolan, D. & Rust, N. C. How does the brain solve visual object recognition? *Neuron* **73**, 415-434 (2012).

3 Bishop, C. M. *Neural networks for pattern recognition*. (Clarendon Press, Oxford, 1995).

4 Barlow, H. B. in *Sensory communication* (ed W. A. Rosenblith) 217-234 (MIT Press, 1961).

5 Atick, J. J. & Redlich, A. N. Convergent algorithm for sensory receptive-field development. *Neural Comput.* **5**, 45-60 (1993).

6 Olshausen, B. A. & Field, D. J. Emergence of simple-cell receptive field properties by learning a sparse code for natural images. *Nature* **381**, 607-609 (1996).

7 Smith, E. C. & Lewicki, M. S. Efficient auditory coding. *Nature* **439**, 978-982 (2006).

8 Friedrich, R. W. & Laurent, G. Dynamic optimization of odor representations in the olfactory bulb by slow temporal patterning of mitral cell activity. *Science* **291**, 889-894 (2001).

9 Friedrich, R. W. & Wiechert, M. T. Neuronal circuits and computations: pattern decorrelation in the olfactory bulb. *FEBS letters* **588**, 2504-2513 (2014).

10 Zhu, P., Frank, T. & Friedrich, R. W. Equalization of odor representations by a network of electrically coupled inhibitory interneurons. *Nature Neurosci.* **16**, 1678-1686 (2013).

11 Friedrich, R. W. & Korsching, S. I. Combinatorial and chemotopic odorant coding in the zebrafish olfactory bulb visualized by optical imaging. *Neuron* **18**, 737-752 (1997).

12 Araneda, R. C., Kini, A. D. & Firestein, S. The molecular receptive range of an odorant receptor. *Nature Neurosci* **3**, 1248-1255 (2000).

13 Mori, K., Takahashi, Y. K., Igarashi, K. M. & Yamaguchi, M. Maps of odorant molecular features in the mammalian olfactory bulb. *Physiol. Rev.* **86**, 409-433 (2006).

14 Friedrich, R. W., Habermann, C. J. & Laurent, G. Multiplexing using synchrony in the zebrafish olfactory bulb. *Nat. Neurosci.* **7**, 862-871 (2004).

15 Niessing, J. & Friedrich, R. W. Olfactory pattern classification by discrete neuronal network states. *Nature* **465**, 47-52 (2010).

16 Gschwend, O. *et al.* Neuronal pattern separation in the olfactory bulb improves odor discrimination learning. *Nat Neurosci* **18**, 1474-1482 (2015).

17 Chu, M. W., Li, W. L. & Komiyama, T. Balancing the Robustness and Efficiency of Odor Representations during Learning. *Neuron* **92**, 174-186 (2016).

18 Yamada, Y. *et al.* Context- and Output Layer-Dependent Long-Term Ensemble Plasticity in a Sensory Circuit. *Neuron* **93**, 1198-1212 e1195 (2017).

19 Banerjee, A. *et al.* An Interglomerular Circuit Gates Glomerular Output and Implements Gain Control in the Mouse Olfactory Bulb. *Neuron* **87**, 193-207 (2015).

20 Willhite, D. C. *et al.* Viral tracing identifies distributed columnar organization in the olfactory bulb. *Proc. Natl. Acad. Sci. USA* **103**, 12592-12597 (2006).

21 Fantana, A. L., Soucy, E. R. & Meister, M. Rat olfactory bulb mitral cells receive sparse glomerular inputs. *Neuron* **59**, 802-814 (2008).

22 Soucy, E. R., Albeanu, D. F., Fantana, A. L., Murthy, V. N. & Meister, M. Precision and diversity in an odor map on the olfactory bulb. *Nat. Neurosci.* **12**, 210-220 (2009).

23 Denk, W. & Horstmann, H. Serial block-face scanning electron microscopy to reconstruct three-dimensional tissue nanostructure. *PLoS Biol* **2**, e329 (2004).

24 Denk, W., Briggman, K. L. & Helmstaedter, M. Structural neurobiology: missing link to a mechanistic understanding of neural computation. *Nat Rev Neurosci* **13**, 351-358 (2012).

25 Wanner, A. A., Genoud, C. & Friedrich, R. W. 3-dimensional electron microscopic imaging of the zebrafish olfactory bulb and dense reconstruction of neurons. *Scientific data* **3**, 160100 (2016).
26 Wanner, A. A., Genoud, C., Masudi, T., Siksou, L. & Friedrich, R. W. Dense EM-based reconstruction of the interglomerular projectome in the zebrafish olfactory bulb. *Nat Neurosci* **19**, 816-825 (2016).
27 Akerboom, J. *et al.* Genetically encoded calcium indicators for multi-color neural activity imaging and combination with optogenetics. *Frontiers in molecular neuroscience* **6**, 2 (2013).
28 Yaksi, E. & Friedrich, R. W. Reconstruction of firing rate changes across neuronal populations by temporally deconvolved Ca^{2+} imaging. *Nature Methods* **3**, 377-383 (2006).
29 Yaksi, E., Judkewitz, B. & Friedrich, R. W. Topological reorganization of odor representations in the olfactory bulb. *PLoS Biol.* **5**, e178 (2007).
30 Carandini, M. & Heeger, D. J. Normalization as a canonical neural computation. *Nat. Rev. Neurosci.* **13**, 51-62 (2011).
31 Wiechert, M. T., Judkewitz, B., Riecke, H. & Friedrich, R. W. Mechanisms of pattern decorrelation by recurrent neuronal circuits. *Nature Neurosci.* **13**, 1003-1010 (2010).
32 Hartline, H. K. & Ratliff, F. Inhibitory interaction of receptor units in the eye of *Limulus*. *J. gen. Physiol.* **40**, 357-376 (1957).
33 Yokoi, M., Mori, K. & Nakanishi, S. Refinement of odor molecule tuning by dendrodendritic synaptic inhibition in the olfactory bulb. *Proc. Natl. Acad. Sci. USA* **92**, 3371-3375 (1995).
34 Cleland, T. A. & Sethupathy, P. Non-topographical contrast enhancement in the olfactory bulb. *BMC Neurosci.* **7**, 7 (2006).
35 Arevian, A. C., Kapoor, V. & Urban, N. N. Activity-dependent gating of lateral inhibition in the mouse olfactory bulb. *Nat. Neurosci.* **11**, 80-87 (2008).
36 Braubach, O. R. *et al.* Experience-dependent versus experience-independent postembryonic development of distinct groups of zebrafish olfactory glomeruli. *J Neurosci* **33**, 6905-6916 (2013).
37 Nishizumi, H. & Sakano, H. Developmental regulation of neural map formation in the mouse olfactory system. *Developmental neurobiology* **75**, 594-607 (2015).
38 Ko, H. *et al.* Functional specificity of local synaptic connections in neocortical networks. *Nature* **473**, 87-91 (2011).
39 Pehlevan, C. & Chklovskii, D. B. in *2015 53rd Annual Allerton Conference on Communication, Control, and Computing (Allerton).* 1458-1465.
40 Zung, J. & Seung, S. A correlation game for unsupervised learning yields computational interpretations of Hebbian excitation, anti-Hebbian inhibition, and synapse elimination. *arXiv*, arXiv:1704.00646v00641 (2017).
41 Kinkhabwala, A. *et al.* A structural and functional ground plan for neurons in the hindbrain of zebrafish. *Proc Natl Acad Sci U S A* **108**, 1164-1169 (2011).
42 Akerboom, J. *et al.* Optimization of a GCaMP calcium indicator for neural activity imaging. *J Neurosci* **32**, 13819-13840 (2012).
43 Westerfield, M. *The zebrafish book. A guide for the laboratory use of zebrafish (Danio rerio)*. 4 edn, (University of Oregon Press, 2000).
44 Li, J. *et al.* Early development of functional spatial maps in the zebrafish olfactory bulb. *J. Neurosci.* **25**, 5784-5795 (2005).
45 Brustein, E., Marandi, N., Kovalchuk, Y., Drapeau, P. & Konnerth, A. "In vivo" monitoring of neuronal network activity in zebrafish by two-photon Ca^{2+} imaging. *Pflügers Arch* **446**, 766-773 (2003).
46 Tabor, R., Yaksi, E., Weislogel, J. M. & Friedrich, R. W. Processing of odor mixtures in the zebrafish olfactory bulb. *J. Neurosci.* **24**, 6611-6620 (2004).

47 Zhu, P., Fajardo, O., Shum, J., Zhang Schärer, Y.-P. & Friedrich, R. W. High-resolution optical control of spatiotemporal neuronal activity patterns in zebrafish using a digital micromirror device. *Nat. Protoc.* **7**, 1410-1425 (2012).
48 Pologruto, T. A., Sabatini, B. L. & Svoboda, K. ScanImage: flexible software for operating laser scanning microscopes. *BioMed. Eng. OnLine* **2**, 13 (2003).
49 Suter, B. A. *et al.* Ephus: multipurpose data acquisition software for neuroscience experiments. *Front. Neural Circuits* **4**, 100 (2010).
50 Keller, P. J., Schmidt, A. D., Wittbrodt, J. & Stelzer, E. H. Digital scanned laser light-sheet fluorescence microscopy (DSLM) of zebrafish and Drosophila embryonic development. *Cold Spring Harbor protocols* **2011**, 1235-1243 (2011).
51 Deerinck, T. J. *et al.* Enhancing serial block-face scanning electron microscopy to enable high resolution 3D nanohistology of cells and tissues. *Microsc. Microanal.* **16**, 1138-1139 (2010).
52 Tapia, J. C. *et al.* High-contrast en bloc staining of neuronal tissue for field emission scanning electron microscopy. *Nat Protoc* **7**, 193-206 (2012).
53 Pinching, A. J. & Powell, T. P. The neuropil of the glomeruli of the olfactory bulb. *J. Cell. Sci.* **9**, 347-377 (1971).
54 Korogod, N., Petersen, C. C. & Knott, G. W. Ultrastructural analysis of adult mouse neocortex comparing aldehyde perfusion with cryo fixation. *eLife* **4**, 10.7554/eLife.05793 (2015).

Acknowledgements We thank B. Hu, A. Lüthi, P. Rupprecht and N. Temiz for comments on the manuscript and the Friedrich group for valuable discussions. C. Genoud made outstanding contributions to the acquisition of electron microscopy data. This work was supported by the Novartis Research Foundation, the Human Frontiers Science Program (HFSP; rgp0015/2010), and the Swiss National Science Foundation (SNF; CRSII3_130470/1, 310030B_152833).

Author contributions A.A.W. participated in all tasks. He analyzed image data, annotated synapses, supervised human annotators, analyzed data, and wrote the manuscript. R.W.F. analyzed data and wrote the manuscript.

Data availability EM data are available under http://doi.org/10.7281/T1MS3QN7. Other data are available from the corresponding author upon request.

437 **Figure Legends**

438 **Fig. 1 | Neuronal organization and computations in the OB. a**, Schematic illustration of whitening in
439 the OB. Top: correlated input patterns with different variance. Bottom: decorrelated output patterns with
440 similar variance. Center: Highly simplified illustration of the OB circuit. MCs receive excitatory input
441 from a single glomerulus and interact via inhibitory INs. Whitening requires multisynaptic interactions
442 between specific subsets of MCs that are mediated by INs and defined by the wiring diagram. **b**, Example
443 of a reciprocal synapse between a MC and an IN. **c**, Reconstructions of a MC (left) and an IN (right).
444 Gray volumes show glomeruli, dots depict synapses, colors denote synapse class (unidirectional non-
445 sensory input [blue], unidirectional output [red], reciprocal [magenta], input from sensory neurons
446 [green]). **d**, Simplified representation of the wiring diagram between MCs and INs (binarized connection
447 strength). Colored matrix elements show MC→IN synapses (blue), MC←IN synapses (orange), and
448 reciprocal synapses (black).

449 **Fig. 2 | Odor-evoked population activity in the OB. a**, Mapping of the six optical image planes selected
450 for calcium imaging onto the EM-based reconstructions of neurons. Thickness of planes shows range of
451 range of drift between trials. **b**, One optical image plane showing raw GCaMP5 fluorescence (left) and the
452 corresponding oblique slice through the EM image stack (right). Dashed line outlines ipsilateral brain
453 hemisphere; continuous white outlines show glomerular neuropil. Tel, telencephalon; OB, olfactory bulb.
454 Region outlined by the red square is enlarged; white dots depict somata in corresponding locations.
455 Bottom left: fluorescence change evoked by an odor stimulus in the same field of view. Arrowheads
456 depict locations of two responsive somata in different images. **c**, Activity of MCs (n = 232) and INs
457 (n = 68) in response to four bile acids (BAs) and four amino acids (AAs) during two time windows, t_1 and
458 t_2. **d**, Left: time courses of odor-evoked activity, pattern correlation (Pearson) and pattern variance.
459 Horizontal bar indicates time of odor stimulation. Black: mean measures across MCs. Gray: individual
460 odors (variance) or odor pairs (correlation). Light blue: mean measures across INs. Correlation was
461 measured only between activity patterns evoked by bile acids because patterns evoked by amino acids
462 were dissimilar already at response onset. Right: Mean measures for MCs during t_1 and t_2. **e**, Matrices
463 showing Pearson correlations between activity patterns across MCs (left) and INs (right) at t_1 and t_2.
464 Odors: TCA, taurocholic acid; GCA, glycocholic acid; GCDCA, glycochenodeoxycholic acid; TDCA,
465 taurodeoxycholic acid; Trp, tryptophan; Phe, phenylalanine; Val, valine; Lys, lysine.

466 **Fig. 3 | Whitening depends on connectivity. a**, Architecture of simulated network with connections
467 between MCs and INs. **b**, Time courses of simulated odor-evoked activity, pattern correlation and pattern
468 variance obtained with different wiring diagrams. Blue: original wiring diagram obtained by circuit

469 reconstruction. Dark red: fully randomized connectivity. Light red: co-permutation of feed-forward
470 (MC→IN) and feed-back (MC←IN) connectivity. Shaded areas show s.d. across different permutations.
471 **c**, Mean pattern correlation and s.d. of pattern variance at t_2. S.d. of pattern variance is normalized to the
472 value observed experimentally at t_1. Horizontal black lines show mean experimental values at t_1.
473 Statistical comparisons of correlation and s.d. of variance were performed using a Mann-Whitney U test
474 and an F-test, respectively. For experimental results and simulations using the reconstructed wiring
475 diagram error bars show s.d. across odor pairs (correlation; bile acids only) or individual odors (s.d. of
476 variance). Significance tests compare values at t_2 to experimental values at t_1. For other simulation results,
477 error bars show s.d. over 20 repetitions. Significance tests compare the mean over repetitions to the mean
478 observed experimentally at t_1. *, $p < 0.05$; **, $p < 0.01$; ***, $p < 0.001$; n.s., not significant. **d**, Top:
479 disynaptic connectivity matrix between MCs ($W_{MC\rightarrow IN} * W_{MC\leftarrow IN}$). Grayscale represents number of
480 disynaptic MC-IN-MC connections (normalized). Bottom: example of a disynaptic connectivity matrix
481 with the same order of MCs after co-permuting $W_{MC\rightarrow IN}$ and $W_{MC\leftarrow IN}$.

482 **Fig. 4 | Tuning-dependent disynaptic connectivity in the OB. a**, Classes of triplet connectivity motifs
483 between MCs and INs. **b**, Left: number of connectivity motifs found in the wiring diagram (considering
484 only MCs with activity measurements; n = 232). Right: z-score quantifying over- or under-representation
485 of motifs as compared to 10,000 independent randomizations. **c**, Number of disynaptic connections
486 between MCs as a function of tuning similarity (signal correlation; binned; mean ± s.e.m.). Black: all
487 MCs (n = 21,528 pairs); gray: excluding MCs without at least one strong odor response (n = 7,875 pairs).
488 **d**, Over- and under-representation of connectivity motifs among MC pairs with high signal correlation
489 ($r_{Signal} > 0.5$; black) and among the remaining pairs ($r_{Signal} \leq 0.5$; gray).

490 **Fig. 5 | Disynaptic connectivity underlying feature suppression. a**, Schematic illustration of contrast
491 enhancement by unidirectional lateral inhibition (left) and down-scaling of cohort activity by reciprocal
492 inhibition (right; feature suppression). Arrow length and grayscale indicate activity. **b**, Example of MC
493 activity patterns evoked by two bile acids (TCA, GCDCA) that were decorrelated between t_1 and t_2. MCs
494 are ranked from top to bottom by their individual contribution to the pattern correlation r at t_1 ($r_{i,t1}$). **c**,
495 Left: average contribution of MCs to all pairwise correlations between activity patterns evoked by bile
496 acids at t_1 and t_2. MCs were ranked by $r_{i,t1}$ for each pair of patterns as in **b**. Sorted vectors of correlation
497 contributions were then averaged over odor pairs. Center, right: Mean bile-acid evoked activity of MCs
498 and mean contribution of MCs to pattern variance. MCs were sorted by $r_{i,t1}$ and averaged as in the left
499 panel. Gray and black curves show correlation contribution, activity, and variance contribution at t_1 and t_2,
500 respectively (same sorting of individual neurons by $r_{i,t1}$ for all curves). Insets enlarge the top part of the

curves (20 MCs with highest $r_{i,t1}$). **d**, Example of disynaptic retrograde tracing of functional cohorts in the wiring diagram. Blue: three MCs with highest $r_{i,t1}$ for the odor pair shown in **b** ("starter MCs"). Green: 12 INs with largest number of synaptic inputs to the starter MCs. Red: 48 MCs with largest number of disynaptic inputs to the starter MCs. Transparency represents the number of synaptic connections. Note that the MCs with strong disynaptic connectivity to the starter MCs include the starter MCs themselves, consistent with pronounced reciprocal connectivity among functionally related MC cohorts. **e**, Disynaptic MC-IN-MC connectivity as a function of correlation contribution at t_1 ($r_{i,t1}$; same ranking as in **b** and **c**). For each pair of bile acids, the 10 MCs with the highest $r_{i,t1}$ were selected as starter cells. Disynaptic inputs from all MCs were then represented in a vector and averaged over odor pairs. Note strong overrepresentation of disynaptic connectivity within the cohort of starter cells (gray shading).

Fig. 6 | Mechanism of whitening analyzed by targeted manipulations of the wiring diagram. a, Mean correlation contribution, activity, and variance contribution of MCs responding to bile acids at t_1 (light blue) and t_2 (dark blue) in simulations. MCs were ranked by the correlation contribution $r_{i,t1}$ observed in experimental data as in Fig. 5b. Insets enlarge the top parts of the curves (20 MCs with highest $r_{i,t1}$) and compare simulation results to experimental data (gray, black) for the same 20 MCs. **b**, Schematic: selective deletion and selective preservation MC cohort connectivity in simulations. **c**, Mean pattern correlation and s.d. of pattern variance (normalized) at t_2 observed in simulations under different conditions. S.d. of pattern variance has been normalized to the experimentally observed value at t_1. Horizontal black lines show mean values at t_1; vertical bars show change relative to t_1. Statistical comparisons of correlation and s.d. of variance were performed using a Mann-Whitney test and an F-test, respectively. Error bars for original wiring diagram show s.d. across odor pairs (correlation; bile acids only) or individual odors (s.d. of variance); significance tests compare values at t_2 to experimental values at t_1. Other error bars show s.d. over means from 20 simulations and significance tests compare the mean over repetitions to the mean observed experimentally at t_1. **, $p < 0.01$; ***, $p < 0.001$; 0.05, $p = 0.05$; n.s., not significant. **d**, Time courses of pattern correlation and of the s.d. of pattern variance in simulations using different wiring diagrams. Shaded area shows s.d. across different permutations. **e**, Mean correlation contribution, activity, and variance contribution of the 20 MCs with the highest $r_{i,t1}$ observed experimentally and in simulations using different wiring diagrams. MCs were ranked by $r_{i,t1}$ observed in experimental data as in **a** and in Fig. 5c (same ranking under all conditions). Gray: t_1; Colored: t_2. Shading shows s.d. across 20 different permutations. Note that the reduction in correlation contribution, activity and variance contribution among MCs with high $r_{i,t1}$ is decreased when connectivity is modified globally or in functional cohorts, but not when connectivity of functional cohorts is preserved.

533 **Supplementary Fig. 1 | Mapping of datasets and activity measurements. a**, Displacement of regions
534 of interest (ROIs) during manual proofreading. ROIs representing somata were mapped from the EM
535 dataset to optical image planes in each trial by an affine transformation that was determined by an
536 iterative landmark-based procedure (Methods). Subsequently, the position of each ROI was adjusted
537 manually on the optical image (n = 7,280 ROIs; six image planes with 11 trials each). The mean
538 displacement (± s.d.) during manual adjustment (proofreading) was small (593 ± 833 nm), implying that
539 automated mapping was highly reliable. **b**, Raw calcium signals (ΔF/F) evoked by eight odors in neurons
540 that were present in all trials (208 MCs and 68 INs). Gray bars indicate odor stimulation.

541 **Supplementary Fig. 2 | Effects of pattern transformations on pattern correlation. a**, Effect of
542 contrast enhancement on the correlation between displaced Gaussian patterns. In such patterns, strongly
543 active units convey stimulus-specific information while weakly active units tend to be non-specific.
544 Contrast enhancement therefore decorrelates patterns because it emphasizes strongly active units and
545 suppresses weakly active units. **b**, Effect of contrast enhancement on the correlation between activity
546 pattern that overlap in strongly active units. Contrast enhancement fails to decorrelate patterns because
547 pattern-specific information is conveyed by moderately or weakly active units. **c**, Patterns that overlap in
548 strongly active units are decorrelated by selective inhibition of strongly active units, which results in
549 contrast reduction. Patterns are decorrelated because the relative contribution of moderately or weakly
550 active units is enhanced. Selective inhibition of strongly active units is generated by dense reciprocal
551 inhibition within cohorts of co-tuned neurons. Inhibitory feedback gain is therefore higher than the
552 average inhibitory feedback gain within a co-tuned cohort when the stimulus feature that activates the
553 cohort is present (feature suppression).

554 **Methods**

555 **Animals and preparation.** Adult zebrafish (Danio rerio) were maintained and bred under standard
556 conditions at 26.5°C. Embryos and larvae of a double-transgenic line
557 (elavl3:GCaMP5 x vglut:DsRed)[41,42] in nacre background were raised at 28.5°C in standard E3 medium[43].

558 Imaging experiments were performed as described previously[44]. In brief, larvae 4 - 5 days post
559 fertilization (dpf) were contained in a small drop of aerated E3 without methylene blue or N-
560 phenylthiourea. Larvae were then paralyzed by addition of 20 µl of fresh mivacurium chloride (Mivacron,
561 GlaxoSmithKline, Munich, Germany)[45] and embedded in 2% low-melting agarose (type VII; Sigma, St
562 Louis, MO, USA) in a perfusion chamber that was inclined by 30° to improve dorsal optical access to the
563 OBs. Agarose covering the noses was carefully removed. A constant stream of E3 (2 ml/min) was
564 delivered through a tube in front of the nose and removed by continuous suction. Throughout the
565 experiment it was ensured that larvae showed normal heartbeat. Larvae that were not fixed for EM
566 recovered from paralysis after a few hours and continued to develop without obvious defects. All animal
567 procedures were performed in accordance with official animal care guidelines and approved by the
568 Veterinary Department of the Canton of Basel-Stadt (Switzerland).

569 **Odor stimulation.** Odor application was performed as described[44]. In brief, odors were delivered to the
570 nose through the E3 medium using a computer-controlled, pneumatically actuated HPLC injection valve
571 (Rheodyne, Rohnert Park, CA, USA). All experiments were carried out at room temperature (~22°C). The
572 odor set comprised one food odor[46], four bile acids (glycochenodeoxycholic acid [GCDCA], taurocholic
573 acid [TCA], taurodeoxycholic acid [TDCA] and glycocholic acid [GCA]; Sigma Aldrich, Munich,
574 Germany) and four amino acids (Trp, Lys, Phe, and Val; Fluka, Neu-Ulm, Germany). Stock solutions of
575 GCDCA, TCA, TDCA, Trp, Lys, Phe and Val at 5×10^{-3} M in E3 were kept refrigerated and diluted
576 1:500 (GCDCA, TCA, TDCA) or 1 : 50 (Trp, Lys, Phe, Val) in aerated E3 medium immediately before
577 the experiment. A stock solution of GCA was prepared in 50% ethanol/50% E3 at 2.5×10^{-3} M,

578 refrigerated, and diluted 1:250 immediately before the experiment. In a given trial, an odor was applied
579 twice for a duration of ~3 s with an inter-stimulus interval of 60 s. Successive trials with different odors
580 were separated by at least 2 min.

581 **Multiphoton calcium imaging.** Multiphoton imaging was performed using a microscope equipped with a
582 mode-locked Ti:sapphire laser (SpectraPhysics) and a 20× objective (NA 1.0, Zeiss) as described[47].
583 GCaMP5 was excited at 910 nm and emission was detected through green (535 ± 25 nm) and red
584 (610 ± 37.5 nm) emission filters in separate channels. Images (256 × 256 pixels) were acquired at 128 ms
585 per frame using SCANIMAGE and EPHUS software[48,49] for a total of 2 min in each trial. Trials were
586 performed sequentially in six focal planes that were separated by approximately 10 µm along the dorso-
587 ventral axis of the OB. The field of view covered the entire cross-section of the OB and parts of the
588 adjacent telencephalon. Ten stimulus trials (nine odors and one E3 control), each including two odor
589 applications, were performed in each focal plane. The order of stimuli was E3, food, GCDCA, TCA,
590 TDCA, GCA, Trp, Lys, Phe, Val. In addition, 2 min of spontaneous activity were recorded in each focal
591 plane. After completion of all trials a stack of images covering the whole olfactory bulb was acquired
592 with a z-step interval of 0.5 µm.

593 **Automated drift correction.** Slow mechanical drift, which may be caused by capillary forces acting on
594 the agarose matrix[50], was corrected for by an automated routine. This routine acquired a small stack
595 (± 3 µm around the focus; 0.5 µm steps) and compared images to a reference by cross-correlation after
596 standardizing image columns and rows. The field of view was then automatically translated in X,Y and Z
597 to maximize the cross-correlation to the reference.

598 **Electron microscopy.** Preparation and imaging of this sample have been described previously (Wanner et
599 al. 2016a, Wanner et al. 2016b). Briefly, tissue was stained *en bloc* with osmium, uranyl acetate and lead
600 aspartate using an established protocol[51,52] with minor modifications and embedded in Epon resin with
601 silver particles to minimize charging[25,26]. Multi-tile images were acquired in high vacuum using a

602 scanning electron microscope (QuantaFEG 200; FEI) equipped with an automated ultramicrotome inside
603 the vacuum chamber (3View; Gatan). Section thickness was 25 nm, pixel size was 9.25 × 9.25 nm^2, and
604 the electron dose was 17.5 $e^- nm^{-2}$. The dataset comprised 4,746 successive sections of which one section
605 was lost due to technical problems. The final stack was cropped to a size of 72.2 × 107.8 × 118.6 μm^3.

606 **Neuron reconstruction and synapse annotation.** Skeletons of all neurons in the OB were reconstructed
607 previously as described[25,26]. Briefly, three independent skeletons of each neuron were generated manually
608 from seed points at somata. Skeletons were converged and mismatches were corrected as described, and
609 high accuracy was verified by measures of precision and recall[26]. Tracing was performed using
610 KNOSSOS (www.knossostool.org) or PyKNOSSOS (https://github.com/adwanner/PyKNOSSOS). Most
611 skeletons were generated by a professional high-throughput image annotation service (www.ariadne.ai).

612 Synapses were annotated manually using PyKNOSSOS in "flight" mode[25]. In the default configuration,
613 PyKNOSSOS displays image data in four viewports: the YX viewport (imaging plane) and three mutually
614 orthogonal viewports of arbitrary orientation. In "flight" mode, the latter is perpendicular to the direction
615 of the current neurite. We found that this "auto-orthogonal" view increases tracing speed and facilitates
616 the identification of branch points and synapses. Annotators followed skeletonized reference neurons
617 along pre-calculated paths to ensure that all neurites were annotated. Most synapses were annotated by a
618 professional image annotation service (www.ariadne.ai).

619 Synapses were identified by a cloud of vesicles that touched the plasma membrane, often at a site of
620 intense staining. Annotators defined synapses by placing three nodes: (1) a node in the presynapse, (2) a
621 node in the synaptic cleft, and (3) a node in the postsynapse. Nodes in the presynapse and postsynapse are
622 skeleton nodes of the pre- and postsynaptic neurons if these skeletons are available. In addition,
623 annotators assigned a confidence level c to each synapse. This confidence level was introduced because
624 synapse identification is not unambiguous; rather, human experts can disagree whether a given structure
625 is a synapse or not even when image quality is high.

626 Synapses were then classified as either “input synapse”, “output synapse”, “sensory synapse” or
627 “unknown”. Input and output synapses are synapses of the reference neuron with the corresponding
628 directions, excluding synapses with sensory neurons. Sensory synapses are input synapses received by the
629 reference neuron from axons of sensory neurons, which were identified by their dark cytoplasm[53].
630 Unknown structures resemble synapses but do not display all characteristic features. These structures
631 often included an intense staining of the membrane but no clearly associated vesicle cloud. We therefore
632 speculate that some of these structures may be gap junctions.

633 We first annotated input and output synapses of all MCs and INs independently of each other. Hence,
634 each synapse should have been encountered twice, once from the presynaptic and once from the
635 postsynaptic side. Synapses of INs were then annotated again by different individuals, resulting in a 3-
636 fold redundancy for each MC-IN synapse. In order to minimize the number of false positives the final
637 wiring diagram retained only those MC-IN synapses that were annotated on the MC and at least once on
638 the IN.

639 Each synapse was assigned a unitary weight. As a consequence, the strength of the connection between
640 two neurons in each direction was given by the number of synapses between this pair of neurons. In
641 addition, we tested two other methods to determine synaptic strength. First, connection strength was
642 binarized such that all connections had strengths 0 or 1, independent of the number of synapses. Second,
643 we defined the weight of a synapse as its mean confidence level c, and the total weight of a connection as
644 the sum of the confidence levels of all synapses. In addition, we tested various confidence thresholds to
645 discard synapses with low confidence before determining the weights. Similar results were obtained with
646 all methods and a wide range of confidence thresholds, implying that results are highly robust.

647 **Correlation between multiphoton and SBEM image stacks.** Mapping of multiphoton to SBEM image
648 data may be complicated by (1) mechanical distortions introduced by the sample preparation procedure,
649 (2) shrinkage due to loss of extracellular space induced by chemical fixation[54], and (3) developmental

650 changes occurring during the approximately three hours between the first calcium imaging trial and the
651 final fixation of the tissue. Initial observations indicated that distortions between image datasets were
652 mostly linear (rotation, translation, shrinkage) while non-linear distortions appeared minimal and
653 developmental changes were negligible. We therefore used an affine transformation to map multiphoton
654 images into the SBEM stack, followed by manual fine adjustment of regions of interest (ROIs) for the
655 extraction of calcium signals.

656 An initial affine transformation matrix was fitted to a set of corresponding points that were selected
657 manually in both datasets. The EM volume was then transformed onto the two-photon images, the
658 position of existing points were optimized manually, and additional pairs of corresponding points were
659 selected. The transform was then re-calculated based on the updated set of landmarks and this procedure
660 was iterated until asymptotic behavior was observed.

661 All somata of the OB were outlined manually in the SBEM dataset and mapped onto the time-averaged
662 multiphoton fluorescence images of each trial, resulting in 7280 mappings of somatic outlines in the
663 SBEM dataset to regions of interest (ROIs) in 66 multiphoton images (11 trials at each of six optical
664 planes). The position of all ROIs was then manually adjusted to optimize the mapping in each trial. The
665 average displacement of ROIs during manual adjustment was small (593 ± 833 nm; mean ± s.d.;
666 Supplementary Fig. 1), demonstrating that the accuracy of the initial affine mapping was already high.

667 **Analysis of calcium signals.** Individual frames of multiphoton image time series were low-pass spatially
668 filtered with a mild 2D Gaussian kernel ($\sigma = 1.2$ pixels). Baseline fluorescence F was calculated as the
669 average fluorescence during a 2 s window before response onset. Traces representing relative changes in
670 fluorescence ($\Delta F/F$) in each ROI were averaged over the two successive odor applications in each trial
671 and band-pass filtered in time using a Butterworth filter with a cutoff frequency of 0.2 times the frame
672 rate. The average population response onset ($t = 0$) was determined manually from all raw $\Delta F/F$ traces
673 and fixed for all trials. Firing rate changes of neurons represented by individual ROIs were estimated by

674 temporal deconvolution of calcium signals as described[28] using standard parameters (τ_{decay} = 3 s,

675 thr_{noise} = 0).

676 Analyses of population activity were restricted to neurons represented by ROIs with a radius ≥2 pixels in

677 all trials (corresponding to an area of 3.14 μm^2; 232 MCs and 68 INs). For network simulations and

678 mechanistic analyses of whitening we considered only the 208 MCs that were pre- and post-synaptic to at

679 least one IN and excluded 24 presumably premature MCs. Population responses to different odors were

680 compared by calculating the Pearson correlation coefficient between the population activity vectors of

681 MCs for the different stimuli at a given time point after response onset.

682 **Network modeling.** Excitatory MCs and inhibitory INs were simulated as threshold-linear units with a

683 state variable representing firing rate. The $r^i(t)$ and $u^j(t)$ representing firing rates of MC *i* and IN *j*,

684 respectively, followed the equations of motion

685 $$\tau_{MC}^i \cdot \frac{dr^i(t)}{dt} = -r^i(t) + G_{sen}^i S^i(t) - G_{inh}^i W_{MC \leftarrow IN} \cdot [u(t) - \theta_{IN}]_+$$

686 $$\tau_{IN}^j \cdot \frac{du^j(t)}{dt} = -u^j(t) + G_{exc}^j W_{IN \leftarrow MC} \cdot [r(t) - \theta_{MC}]_+$$

687 where the vectors r θ_{MC} and θ_{IN} are firing thresholds, $W_{MC \leftarrow IN}$ and $W_{IN \leftarrow MC}$ correspond to the

688 reconstructed IN-to-MC and MC-to-IN connectivity weight matrices, respectively, and the vectors $r(t)$

689 and $u(t)$ represent the firing rates of the MC and IN, respectively. $[]_+$ denotes half-wave rectification:

690 $$[x(t)]_+ = \begin{cases} 0, & x(t) < 0 \\ x(t), & x(t) \geq 0 \end{cases}$$

691 τ_{MC}^i and τ_{IN}^j are the time constants for the individual MCs and INs, respectively. G_{sen}^i, G_{inh}^i and G_{exc}^j are

692 the individual scaling factor for sensory, inhibitory and excitatory input, respectively. To account for the

693 natural variability in biological systems, the parameter values for each of the cells in each of the

694 individual simulation runs were drawn from a Gaussian distribution with a standard deviation of 1% of
695 the distribution mean. The distribution means of the different parameters were:

696 G_{sen} = 2.5, G_{exc} = 3.25, G_{inh} = 5.5, θ_{MC} = 3.6, θ_{IN} = 110, τ_{MC} = 1, τ_{IN} = 250;

697 The time course of sensory input $S^i(t)$ was modelled as difference of exponentials as described
698 previously[31]:

699 $\tilde{s}(t) = -a_{j,\infty} + \frac{a_{j,\infty}}{1-\alpha}(1 - e^{-\tau_r t} - \alpha + \alpha e^{-\tau_d t})$ with $\alpha = 0.8, \tau_r = {}^{1}/_{150}, \tau_d = {}^{1}/_{600}, a_{j,\infty} = {}^{1}/_{150}$

700 To model $S_i(t)$, the individual sensory input of MC *i*, we used its experimentally measured activity
701 $\hat{a}_i$ during t_I and modulated the time course according to $\tilde{s}(t)$:

702 $S_i(t) = \hat{a}_i \frac{\tilde{s}(t)}{\tilde{s}_{max}}$, where $\tilde{s}_{max} = \max_{t \geq 0}(\tilde{s}(t))$

703 The differential equations were solved in MATLAB with a fixed step size of 1 millisecond using a first
704 degree Newton-Cotes integration scheme or using an adaptive step size embedded Runge-Kutta-Fehlberg
705 (4, 5) scheme. Both integration schemes lead to qualitatively very similar results, and therefore the former
706 method was used for simplicity for the simulated data shown here.

707 In an iterative, semi-automated parameter search, we identified a suitable parameter range that fulfilled
708 the following criteria:

709 (1) The peak firing rates of individual neurons does not exceed a physiologically realistic range (< 200
710 Hz).

711 (2) The strength of inhibition is appropriate to reproduce the time course of the average population
712 activity, correlation and variance.

713 (3) The activity, correlation contribution and variance contribution of individual MCs at t_1 and t_2 is in
714 good correspondence to experimental measurements.

715 Parameters for which these criteria were fulfilled were found by parameter variations in pilot studies.
716 Results were usually robust against variations of each parameter by ±50% around the values reported
717 above.

718 **Analysis of triplet motifs.** Occurrences of disynaptic MC-IN-MC motifs were counted after binarizing
719 connections. We enumerated all neuron triplet combinations in the reconstructed wiring diagram and
720 tested for graph isomorphism against all 4 disynaptic motif types. The obtained motif counts were
721 compared against a reference model where the forward and backward connectivity of the MCs were
722 permuted independently while maintaining the node count and edge density (n = 10 000 permutations).
723 The z-scores and p-values were obtained by computing the mean and standard deviation of each motif
724 type in the permuted networks.

725 To compare the motif frequency as a function of the pairwise tuning similarity, we divided the MC pairs
726 into two groups, one with similar tuning ($r_{signal} > 0.5$) and one with dissimilar tuning ($r_{signal} \leq 0.5$) and
727 counted the occurrences of MC-IN-MC motifs in each group. We then compared the motif counts against
728 a reference model where we permuted the pairwise tuning similarity between MCs and regrouped them
729 by tuning similarity ($r_{signal} > 0.5$ versus $r_{signal} \leq 0.5$) while maintaining the same network topology
730 (n = 10 000 permutations). The z-scores and p-values were then obtained by computing the mean and
731 standard deviation of each motif type in the permuted groups (Fig 4d).

732 **Additional analyses.** The contribution of individual MCs to the Pearson correlation coefficient

733 $$r = \frac{1}{n-1}\sum_{i=1}^{n}\left(\frac{x_i - \bar{x}}{sd_x}\right)\left(\frac{y_i - \bar{y}}{sd_y}\right)$$

between population activity patterns was calculated by determining the summand $\left(\frac{x_i - \bar{x}}{sd_x}\right)\left(\frac{y_i - \bar{y}}{sd_y}\right)$ for each MC. Similarly, the contribution of individual MCs to the variance

$$sd_x^2 = \frac{1}{n-1}\sum_{i=1}^{n}(x_i - \bar{x})^2$$

of the population activity patterns was calculated by determining the summand $(x_i - \bar{x})^2$ for each MC. Here, x_i and y_i are responses of MCs to odors x and y, sd_x and sd_y are the standard deviations of population responses to odors x and y, and n is the total number of MCs in the population.

Statistical significance was tested using a non-parametric Mann-Whitney U test unless noted otherwise.

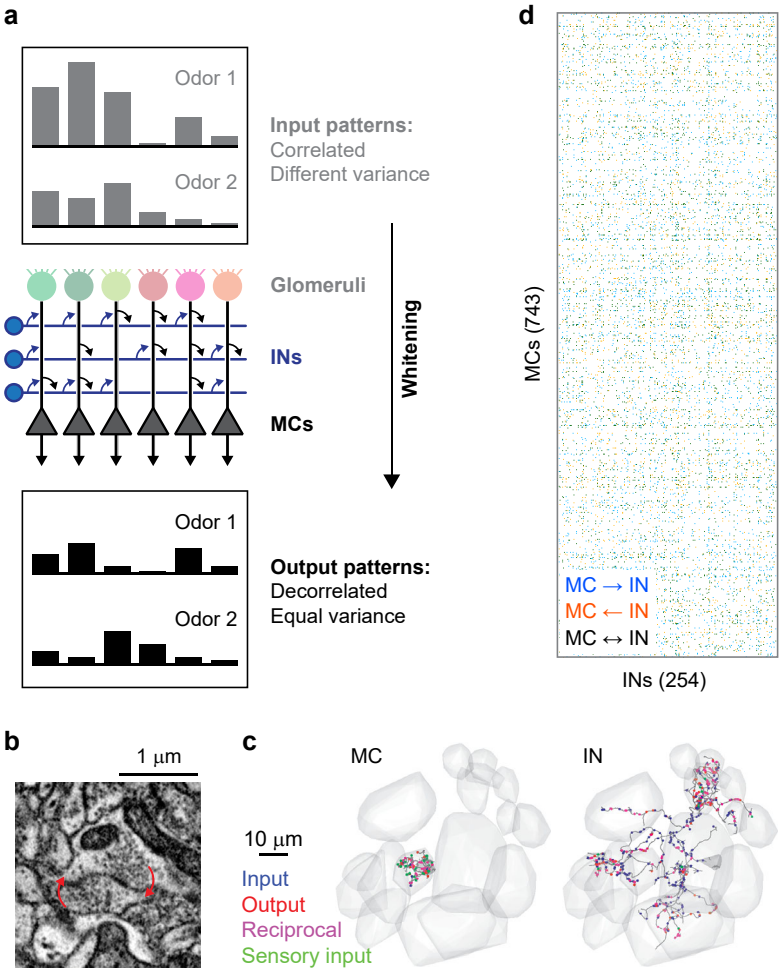

Fig. 1 | Neuronal organization and computations in the OB. a, Schematic illustration of whitening in the OB. Top: correlated input patterns with different variance. Bottom: decorrelated output patterns with similar variance. Center: Highly simplified illustration of the OB circuit. MCs receive excitatory input from a single glomerulus and interact via inhibitory INs. Whitening requires multisynaptic interactions between specific subsets of MCs that are mediated by INs and defined by the wiring diagram. **b**, Example of a reciprocal synapse between a MC and an IN. **c**, Reconstructions of a MC (left) and an IN (right). Gray volumes show glomeruli, dots depict synapses, colors denote synapse class (unidirectional non-sensory input [blue], unidirectional output [red], reciprocal [magenta], input from sensory neurons [green]). **d**, Simplified representation of the wiring diagram between MCs and INs (binarized connection strength). Colored matrix elements show MC→IN synapses (blue), MC←IN synapses (orange), and reciprocal synapses (black).

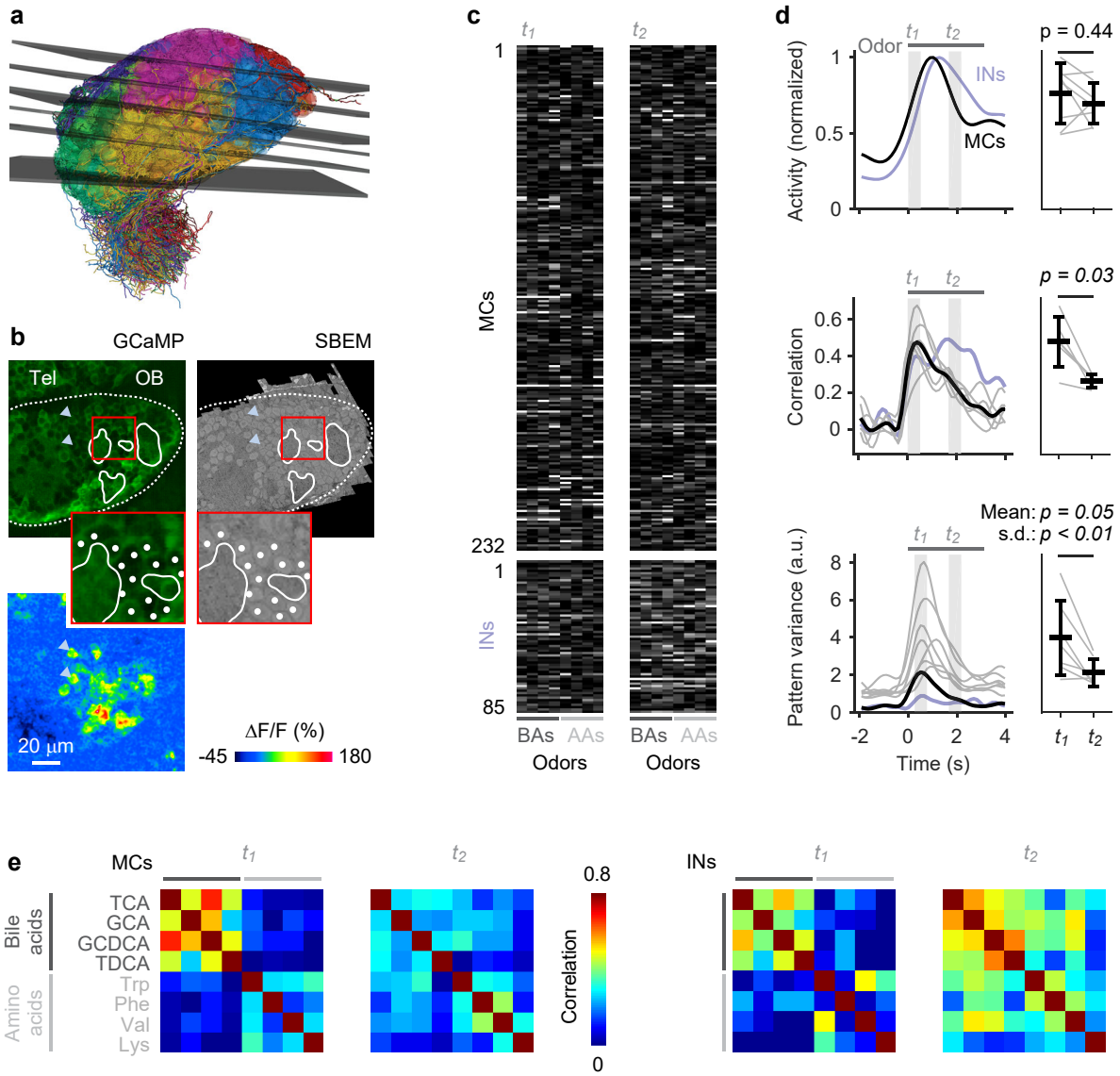

Fig. 2 | Odor-evoked population activity in the OB. a, Mapping of the six optical image planes selected for calcium imaging onto the EM-based reconstructions of neurons. Thickness of planes shows range of range of drift between trials. **b**, One optical image plane showing raw GCaMP5 fluorescence (left) and the corresponding oblique slice through the EM image stack (right). Dashed line outlines ipsilateral brain hemisphere; continuous white outlines show glomerular neuropil. Tel, telencephalon; OB, olfactory bulb. Region outlined by the red square is enlarged; white dots depict somata in corresponding locations. Bottom left: fluorescence change evoked by an odor stimulus in the same field of view. Arrowheads depict locations of two responsive somata in different images. **c**, Activity of MCs (n = 232) and INs (n = 68) in response to four bile acids (BAs) and four amino acids (AAs) during two time windows, t_1 and t_2. **d**, Left: time courses of odor-evoked activity, pattern correlation (Pearson) and pattern variance. Horizontal bar indicates time of odor stimulation. Black: mean measures across MCs. Gray: individual odors (variance) or odor pairs (correlation). Light blue: mean measures across INs. Correlation was measured only between activity patterns evoked by bile acids because patterns evoked by amino acids were dissimilar already at response onset. Right: Mean measures for MCs during t_1 and t_2. **e**, Matrices showing Pearson correlations between activity patterns across MCs (left) and INs (right) at t_1 and t_2. Odors: TCA, taurocholic acid; GCA, glycocholic acid; GCDCA, glycochenodeoxycholic acid; TDCA, taurodeoxycholic acid; Trp, tryptophan; Phe, phenylalanine; Val, valine; Lys, lysine.

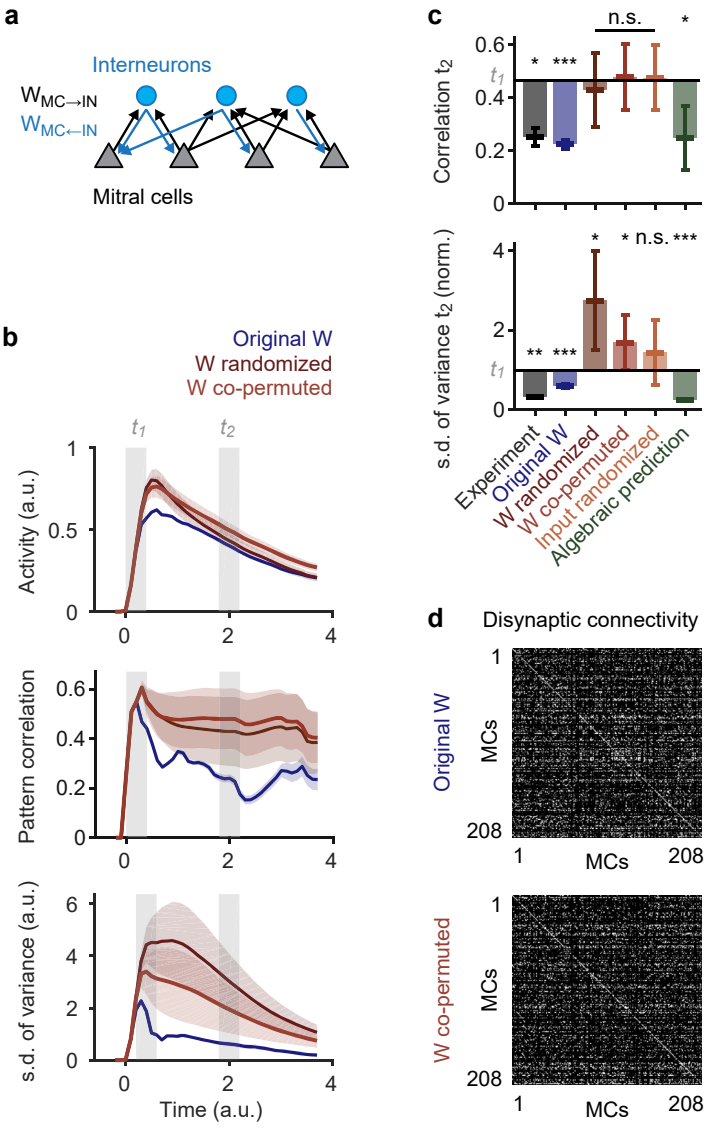

Fig. 3 | Whitening depends on connectivity. a, Architecture of simulated network with connections between MCs and INs. **b**, Time courses of simulated odor-evoked activity, pattern correlation and pattern variance obtained with different wiring diagrams. Blue: original wiring diagram obtained by circuit reconstruction. Dark red: fully randomized connectivity. Light red: co-permutation of feed-forward (MC→IN) and feed-back (MC←IN) connectivity. Shaded areas show s.d. across different permutations. **c**, Mean pattern correlation and s.d. of pattern variance at t_2. S.d. of pattern variance is normalized to the value observed experimentally at t_1. Horizontal black lines show mean experimental values at t_1. Statistical comparisons of correlation and s.d. of variance were performed using a Mann-Whitney U test and an F-test, respectively. For experimental results and simulations using the reconstructed wiring diagram error bars show s.d. across odor pairs (correlation; bile acids only) or individual odors (s.d. of variance). Significance tests compare values at t_2 to experimental values at t_1. For other simulation results, error bars show s.d. over 20 repetitions. Significance tests compare the mean over repetitions to the mean observed experimentally at t_1. *, $p < 0.05$; **, $p < 0.01$; ***, $p < 0.001$; n.s., not significant. **d**, Top: disynaptic connectivity matrix between MCs ($W_{MC\rightarrow IN} * W_{MC\leftarrow IN}$). Grayscale represents number of disynaptic MC-IN-MC connections (normalized). Bottom: example of a disynaptic connectivity matrix with the same order of MCs after co-permuting $W_{MC\rightarrow IN}$ and $W_{MC\leftarrow IN}$.

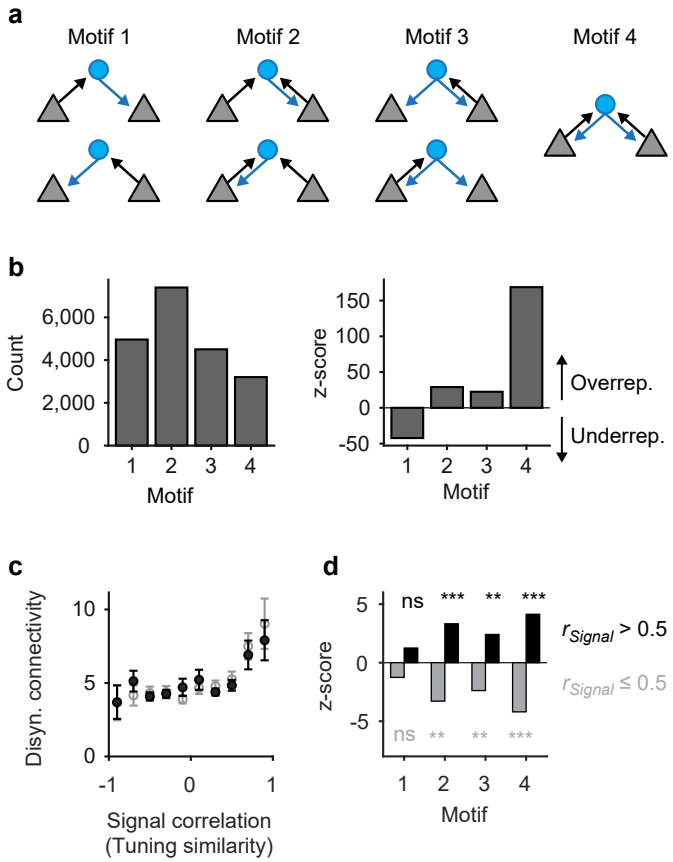

Fig. 4 | Tuning-dependent disynaptic connectivity in the OB. a, Classes of triplet connectivity motifs between MCs and INs. **b**, Left: number of connectivity motifs found in the wiring diagram (considering only MCs with activity measurements; n = 232). Right: z-score quantifying over- or under-representation of motifs as compared to 10,000 independent randomizations. **c**, Number of disynaptic connections between MCs as a function of tuning similarity (signal correlation; binned; mean ± s.e.m.). Black: all MCs (n = 21,528 pairs); gray: excluding MCs without at least one strong odor response (n = 7,875 pairs). **d**, Over- and under-representation of connectivity motifs among MC pairs with high signal correlation ($r_{Signal} > 0.5$; black) and among the remaining pairs ($r_{Signal} \leq 0.5$; gray).

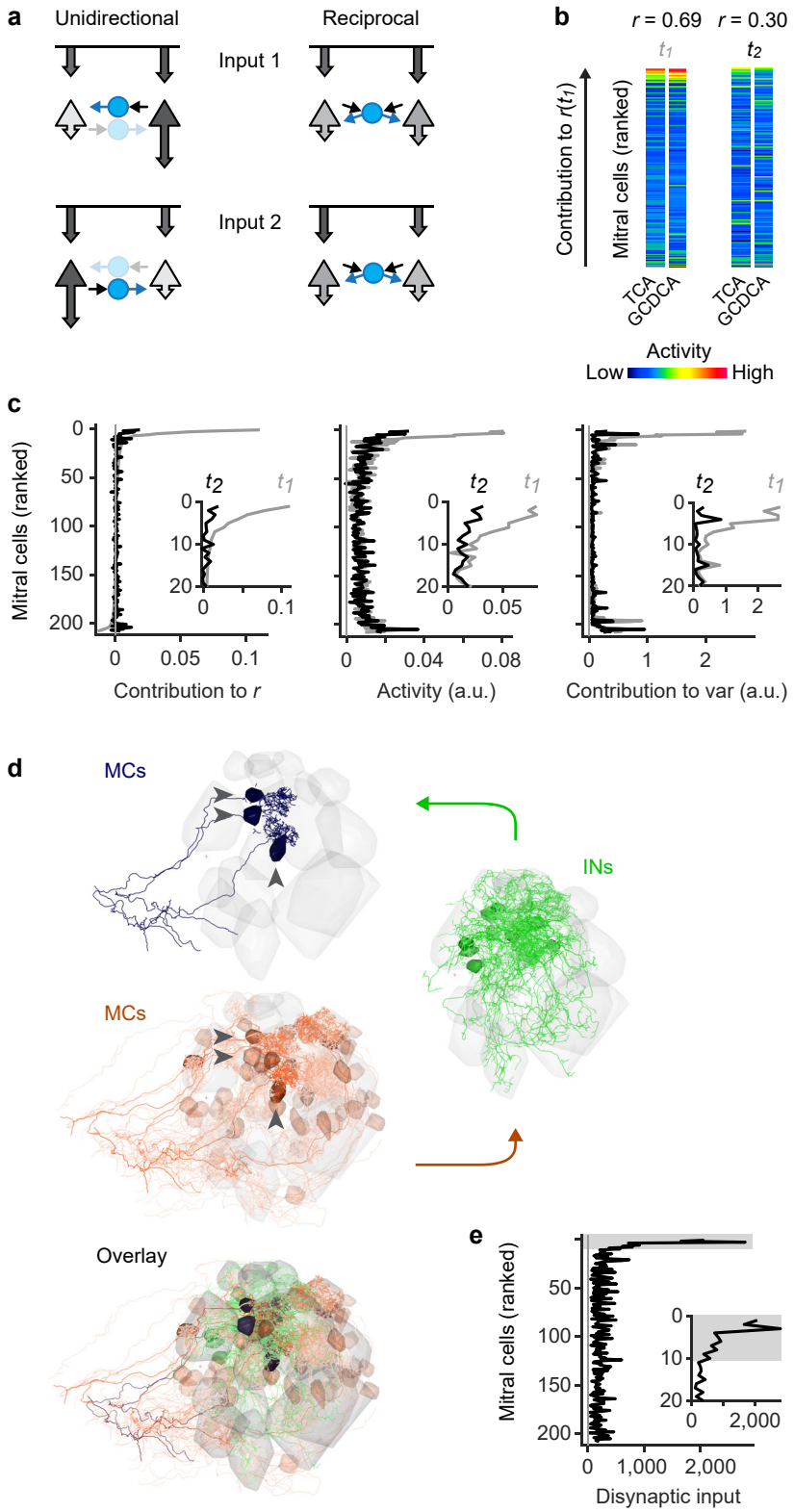

Fig. 5 | Disynaptic connectivity underlying feature suppression. a, Schematic illustration of contrast enhancement by unidirectional lateral inhibition (left) and down-scaling of cohort activity by reciprocal inhibition (right; feature suppression). Arrow length and grayscale indicate activity. **b**, Example of MC activity patterns evoked by two bile acids (TCA, GCDCA) that were decorrelated between t_1 and t_2. MCs are ranked from top to bottom by their individual contribution to the pattern correlation r at t_1 ($r_{i,t1}$). **c**, Left: average contribution of MCs to all pairwise correlations between activity patterns evoked by bile acids at t_1 and t_2. MCs were ranked by $r_{i,t1}$ for each pair of patterns as in **b**. Sorted vectors of correlation contributions were then averaged over odor pairs. Center, right: Mean bile-acid evoked activity of MCs and mean contribution of MCs to pattern variance. MCs were sorted by $r_{i,t1}$ and averaged as in the left panel. Gray and black curves show correlation contribution, activity, and variance contribution at t_1 and t_2, respectively (same sorting of individual neurons by $r_{i,t1}$ for all curves). Insets enlarge the top part of the curves (20 MCs with highest $r_{i,t1}$). **d**, Example of disynaptic retrograde tracing of functional cohorts in the wiring diagram. Blue: three MCs with highest $r_{i,t1}$ for the odor pair shown in **b** ("starter MCs"). Green: 12 INs with largest number of synaptic inputs to the starter MCs. Red: 48 MCs with largest number of disynaptic inputs to the starter MCs. Transparency represents the number of synaptic connections. Note that the MCs with strong disynaptic connectivity to the starter MCs include the starter MCs themselves, consistent with pronounced reciprocal connectivity among functionally related MC cohorts. **e**, Disynaptic MC-IN-MC connectivity as a function of correlation contribution at t_1 ($r_{i,t1}$; same ranking as in **b** and **c**). For each pair of bile acids, the 10 MCs with the highest $r_{i,t1}$ were selected as starter cells. Disynaptic inputs from all MCs were then represented in a vector and averaged over odor pairs. Note strong overrepresentation of disynaptic connectivity within the cohort of starter cells (gray shading).

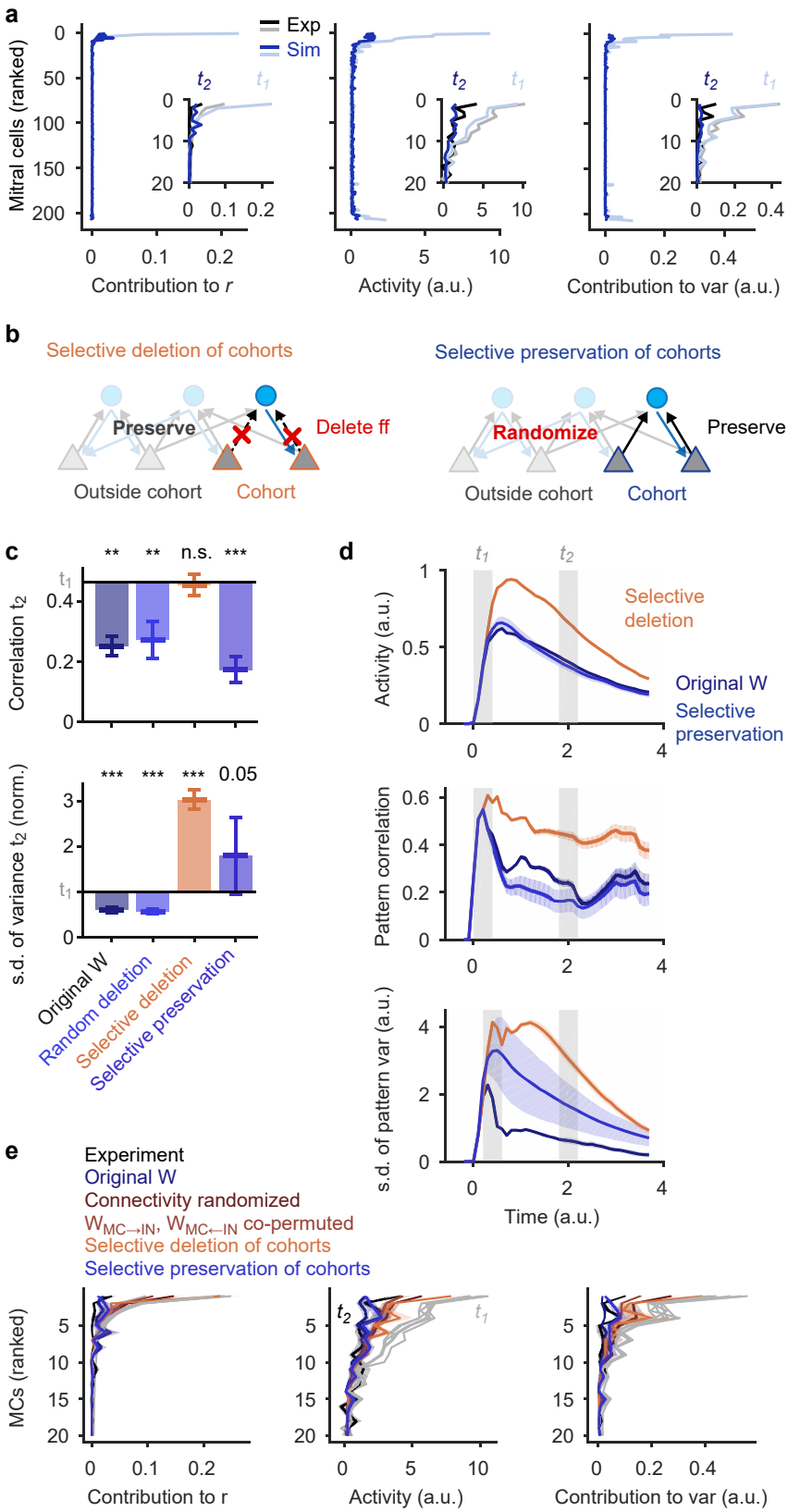

Fig. 6 | Mechanism of whitening analyzed by targeted manipulations of the wiring diagram. a, Mean correlation contribution, activity, and variance contribution of MCs responding to bile acids at t_1 (light blue) and t_2 (dark blue) in simulations. MCs were ranked by the correlation contribution $r_{i,tI}$ observed in experimental data as in **Fig. 5c**. Insets enlarge the top parts of the curves (20 MCs with highest $r_{i,tI}$) and compare simulation results to experimental data (gray, black) for the same 20 MCs. **b**, Schematic: selective deletion and selective preservation MC cohort connectivity in simulations. **c**, Mean pattern correlation and s.d. of pattern variance (normalized) at t_2 observed in simulations under different conditions. S.d. of pattern variance has been normalized to the experimentally observed value at t_1. Horizontal black lines show mean values at t_1; vertical bars show change relative to t_1. Statistical comparisons of correlation and s.d. of variance were performed using a Mann-Whitney test and an F-test, respectively. Error bars for original wiring diagram show s.d. across odor pairs (correlation; bile acids only) or individual odors (s.d. of variance); significance tests compare values at t_2 to experimental values at t_1. Other error bars show s.d. over means from 20 simulations and significance tests compare the mean over repetitions to the mean observed experimentally at t_1. **, $p < 0.01$; ***, $p < 0.001$; 0.05, $p = 0.05$; n.s., not significant. **d**, Time courses of pattern correlation and of the s.d. of pattern variance in simulations using different wiring diagrams. Shaded area shows s.d. across different permutations. **e**, Mean correlation contribution, activity, and variance contribution of the 20 MCs with the highest $r_{i,tI}$ observed experimentally and in simulations using different wiring diagrams. MCs were ranked by $r_{i,tI}$ observed in experimental data as in **a** and in **Fig. 5c** (same ranking under all conditions). Gray: t_1; Colored: t_2. Shading shows s.d. across 20 different permutations. Note that the reduction in correlation contribution, activity and variance contribution among MCs with high $r_{i,tI}$ is decreased when connectivity is modified globally or in functional cohorts, but not when connectivity of functional cohorts is preserved.

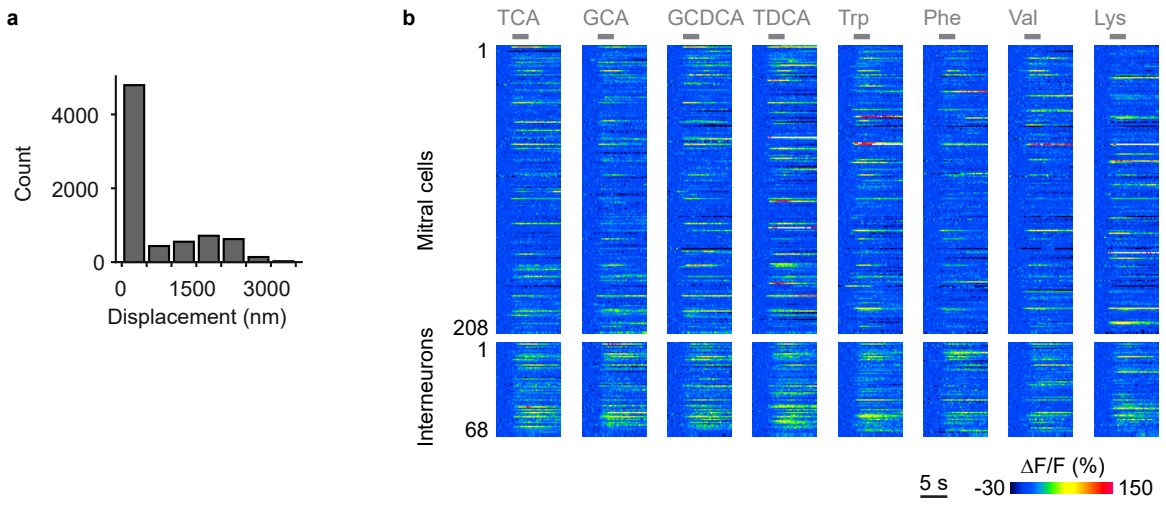

Supplementary Fig.1 | Mapping of datasets and activity measurements. a, Displacement of regions of interest (ROIs) during manual proofreading. ROIs representing somata were mapped from the EM dataset to optical image planes in each trial by an affine transformation that was determined by an iterative landmark-based procedure (Methods). Subsequently, the position of each ROI was adjusted manually on the optical image (n = 7,280 ROIs; six image planes with 11 trials each). The mean displacement (± s.d.) during manual adjustment (proofreading) was small (593 ± 833 nm), implying that automated mapping was highly reliable. **b**, Raw calcium signals (ΔF/F) evoked by eight odors in neurons that were present in all trials (208 MCs and 68 INs). Gray bars indicate odor stimulation.

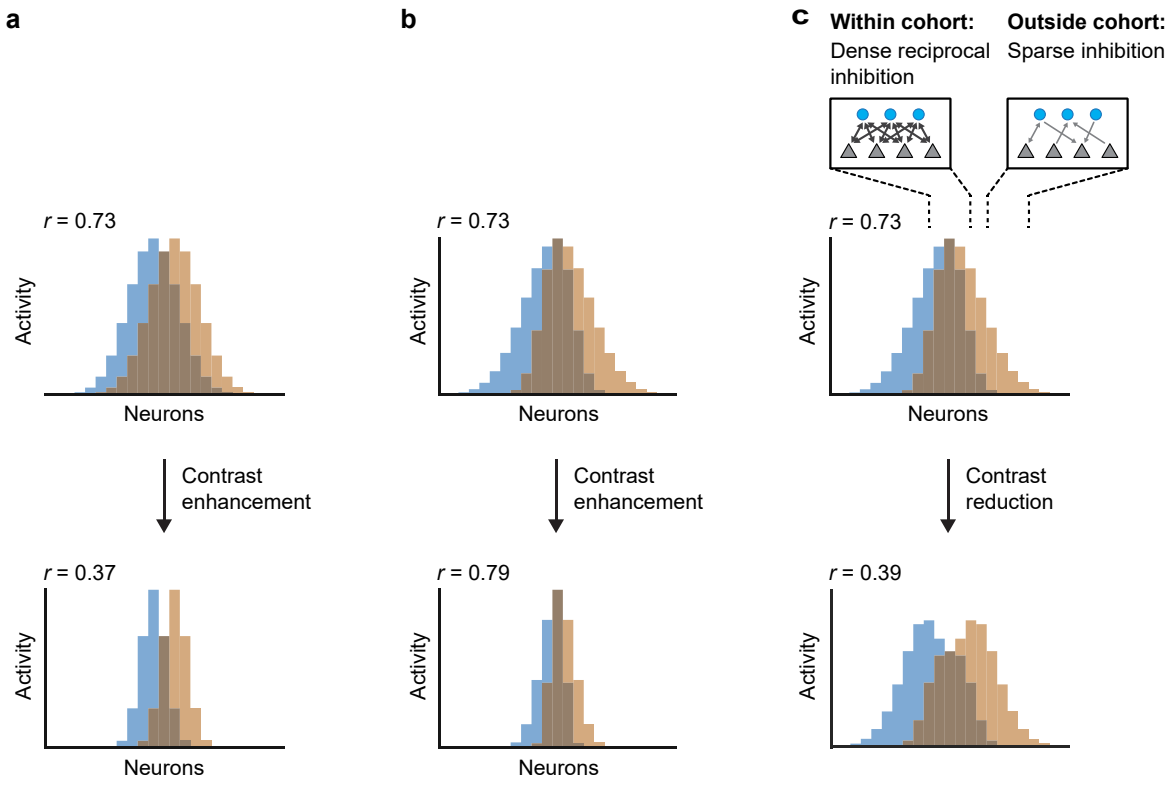

Supplementary Fig.2 | Effects of pattern transformations on pattern correlation. a, Effect of contrast enhancement on the correlation between displaced Gaussian patterns. In such patterns, strongly active units convey stimulus-specific information while weakly active units tend to be non-specific. Contrast enhancement therefore decorrelates patterns because it emphasizes strongly active units and suppresses weakly active units. **b**, Effect of contrast enhancement on the correlation between activity pattern that overlap in strongly active units. Contrast enhancement fails to decorrelate patterns because pattern-specific information is conveyed by moderately or weakly active units. **c**, Patterns that overlap in strongly active units are decorrelated by selective inhibition of strongly active units, which results in contrast reduction. Patterns are decorrelated because the relative contribution of moderately or weakly active units is enhanced. Selective inhibition of strongly active units is generated by dense reciprocal inhibition within cohorts of co-tuned neurons. Inhibitory feedback gain is therefore higher than the average inhibitory feedback gain within a co-tuned cohort when the stimulus feature that activates the cohort is present (feature suppression).